ORIGINAL PAPER

Geochemistry of rhodonite in the Luziyuan Pb – Zn skarn deposit, Southwestern China

Yulong Yang[1] · Lin Ye[2] · Wei Gao[2,3] · Tan Bao[2,3] · Zhenli Li[2,3] · Yusi Hu[2,3] · Chen Wei[2,3]

Abstract

The Luziyuan skarn deposit is the second largest Pb − Zn deposit in the Baoshan block, Yunnan Province, Southwestern China. Rhodonite is a widespread skarn mineral in the host rock, occurring as coarse-grained crystals and veins, and is closely associated with Pb − Zn mineralization. In-situ elemental analysis of rhodonite from three levels (1220 m, 1265 m and 1495 m above sea level) by laser ablation-inductively coupled plasma-mass spectrometry and Sm − Nd isotopic dating of the rhodonite − calcite pair were conducted to constrain the compositions and the timing of Pb − Zn mineralization. The new Sm − Nd isotopic data reveal that the Luziyuan deposit formed during the Early Jurassic (183 ± 2.3 Ma; MSWD = 0.72). These chronological constraints, combined with regional tectonic evolution, suggest that the Luziyuan Pb − Zn mineralization is genetically linked to eastward subduction of the Shan Boundary Ocean beneath the Baoshan block during the Meso-Tethys period. Furthermore, all examined rhodonite samples contain relatively high concentrations of MnO (34.7 − 43.0 wt%) and Zn (536 − 2117 ppm), but generally low contents of FeO (1.07 − 6.08 wt%), Cu, Co, Ni, Ga, Mo, Sn, W and Pb. A positive correlation between Zn and MnO contents among different skarn deposits and nearly chondritic Y/Ho ratio (~ 28) in the Luziyuan rhodonite suggests that this mineral formed from magmatic fluids and its Zn enrichment was controlled by the fluid chemistry. The same data also suggest that Zn-rich rhodonite in skarns may be used as an indicator mineral for Zn exploration when combined with other geological, geophysical, and geochemical criteria.

Keywords Rhodonite · LA-ICP-MS · Sm − Nd geochronology · Luziyuan Pb − Zn deposit · Southwestern China

Introduction

Rhodonite has rarely been reported from Pb − Zn skarns since Abrecht (1985) and Meinert (1987) identified this mineral in the Groundhog Pb–Zn deposit and Empire Pb − Zn − Cu deposit in the USA. These researchers mainly focused on the relationship between its texture and genesis, e.g., rhodonite lamellae within clinopyroxene, caused

by Mn − Ca ion exchange reaction between rhodonite and clinopyroxene, and euhedral rhodonite occurring together with calcite + quartz, which was interpreted to indicate increasing CO_2 activity in the skarn fluid. More recently, some workers (Zhao et al. 2003; Meinert et al. 2005; Chen et al. 2017) noticed a close relationship between manganoan pyroxenoids (e.g., rhodonite) and lead–zinc mineralization in the Pb − Zn skarn deposit; however, no attention has been paid to the reasons behind this relationship.

A Zn-rich rhodonite variety (fowlerite) from Franklin, New Jersey (USA), has been reported by Nelson and Griffen (2005). Based on X-ray structure refinements, Zn was found to preferentially occupy the fivefold-coordinated M4 site in fowlerite. As a Ca-bearing silicate mineral, rhodonite can incorporate a certain amount of REE substituting for Ca (Pan and Fleet 1996). These crystallographic and chemical characteristics make rhodonite a useful geochemical tracer. The Sm − Nd geochronometry of Ca-bearing minerals (e.g., fluorite, calcite, and scheelite) has been developed to solve the long-standing problem of directly dating hydrothermal

✉ Lin Ye
  yelin@vip.gyig.ac.cn

1 College of Earth Sciences, Chengdu University of Technology, Chengdu 610059, China

2 State Key Laboratory of Ore Deposit Geochemistry, Institute of Geochemistry, Chinese Academy of Sciences, Guiyang 550081, China

3 University of Chinese Academy of Sciences, Beijing 100049, China

deposits (e.g., Mississippi Valley − type deposits, Chesley et al. 1994; Muruntau Au(− W) deposit in Uzbekistan, Kempe et al. 2001; Shuiyindong Carlin − type gold deposit in China, Su et al. 2009). Rhodonite rarely occurs in distal skarn Pb − Zn deposits, and its precipitation is often closely related to the deposition of Pb + Zn (Meinert et al. 2005). However, Sm − Nd geochronometry to constrain the timing of Pb − Zn mineralization has not yet been applied to rhodonite.

With 1.9 Mt of Pb + Zn reserves discovered prior to 2006, the Luziyuan mine is the second largest deposit of this type in the Baoshan–Zhenkang block, Yunnan Province, southwestern China, after the Hetaoping deposit (> 2 Mt). Previous studies of the former deposit have paid little attention to skarn minerals (e.g., rhodonite), with the exception of a few studies that examined the major and trace element characteristics of rhodonite by bulk analysis of a single rhodonite sample using inductively coupled plasma-mass spectrometry (ICP-MS) (i.e. Deng et al. 2013, 2016). Because these studies were based on bulk analytical techniques and handpicked grains, it was not possible to constrain the distribution patterns of trace elements in rhodonite and thus elucidate mineralization processes responsible for the Luziyuan deposit.

This research paper presents in-situ trace-element analyses of rhodonite by laser ablation-inductively coupled plasma-mass spectrometry (LA-ICP-MS), and a new Sm − Nd age determination for rhodonite associated with Pb − Zn mineralization at Luziyuan. This contribution aims to provide insights into the causes of incorporation of certain trace elements into rhodonite and their significance for the Zn mineralization in the study area. Given the poorly constrained age of the Luziyuan deposit, this study reports the first reliable geochronological data, providing new constraints on the timing of Pb − Zn mineralization and its relationship to the regional tectonics.

Geological setting

Regional geology

The southern part of the Sanjiang region consists of the South China, Simao–Indochina and Sibumasu terranes. These areas are separated by the Ailaoshan and Changning–Menglian sutures that formed through the closure of the Tethys Ocean (Fig. 1a, b; Deng et al. 2014). They record the opening and closure of the Paleo-Tethys (Devonian-Triassic) Ocean, formed after the rifting of various microcontinental blocks from Gondwana (Usuki et al. 2012; Metcalfe 2013). Based on the known ophiolitic sutures, two main branches of the Paleo-Tethys Ocean have been recognized in this area, which from east to west are as follows (Deng et al. 2014): Ailaoshan Ocean (suture

5 in Fig. 1b) and the Changning-Menglian Ocean (suture 4 in Fig. 1b). During the Late Carboniferous (ca. 305 Ma), the eastward subduction of the Changning-Menglian Ocean and the westward subduction of the Ailaoshan Ocean resulted in the formation of multiple, sub-parallel Paleozoic continental arc terranes on both sides of the Simao block (Deng et al. 2014). Following the closure of the two oceans, three blocks (Sibumasu, Simao, and South China) amalgamated during the Triassic (ca. 235 Ma), which produced some peraluminous granitoids associated with skarn-type Sn − W deposits in the western part of the Simao block (e.g., the Songshan skarn-type Sn deposit and the Bulangshan skarn–greisen Sn deposit, Wang et al. 2014).

The Luxi rift within the Sibumasu block opened during the Middle Permian creating the Baoshan and Tengchong blocks, but it did not form an ocean basin and is thus considered a failed continental rift of the Paleo-Tethys Ocean (Deng et al. 2014). This rift closed during the middle Triassic and the Tengchong and Baoshan blocks rejoined. The eastward subduction of the Meso-Tethys Ocean (namely the Shan boundary ocean) beneath the merged Tengchong-Baoshan block from the middle Triassic resulted in widespread early-Cretaceous granitoids and associated skarn-type Pb–Zn deposits (e.g., the Hetaoping, Luziyuan, and Jinchanghe deposits, Deng et al. 2014).

Early Paleozoic granitoids, ranging in age from 500 to 470 Ma, occur scattered throughout the southern portion of the Baoshan block and include Pinghe granite (486 − 480 Ma, Dong et al. 2012) and Mengmao granite (455 Ma, Xiong et al. 2012). Permian magmatism in the Baoshan block is exemplified by the Muchang A-type granitic pluton, which yielded a zircon U–Pb age of 266 ± 5.4 Ma (Ye et al. 2010). Cretaceous magmatism in the Baoshan block is represented by the Zhibenshan and Kejie granites. Zircon from these two plutons yield a U–Pb age of 126.7 ± 1.6 Ma and 93 ± 1.3 Ma, respectively (Tao et al. 2010). Previous studies (Tao et al. 2010; Zhu et al. 2011; Huang et al. 2014) using Rb–Sr methods reported Late Yanshanian mineralization ages for skarn Pb − Zn deposits (e.g., 141.9 ± 2.6 Ma for the Luziyuan deposit; 116.1 ± 3.9 Ma for the Hetaoping deposit; 117.0 ± 2.4–120.3 ± 5.1 Ma for the Jinchanghe deposit) in the Baoshan block. These authors considered that these skarn Pb − Zn deposits are related to some concealed, Late Yanshanian intermediate-acidic intrusive rocks, which seemed supported by negative gravity and magnetic anomalies identified in the Baoshan region (Li and Mo 2001; Zhao et al. 2002; Dong and Chen 2007). Noticeably, a non-exposed intermediate-acidic intrusion in the Baoshan area is considered as the "sister" of the Muchang A-type granite and a product of Mid-Permian igneous activity (Ye et al. 2010).
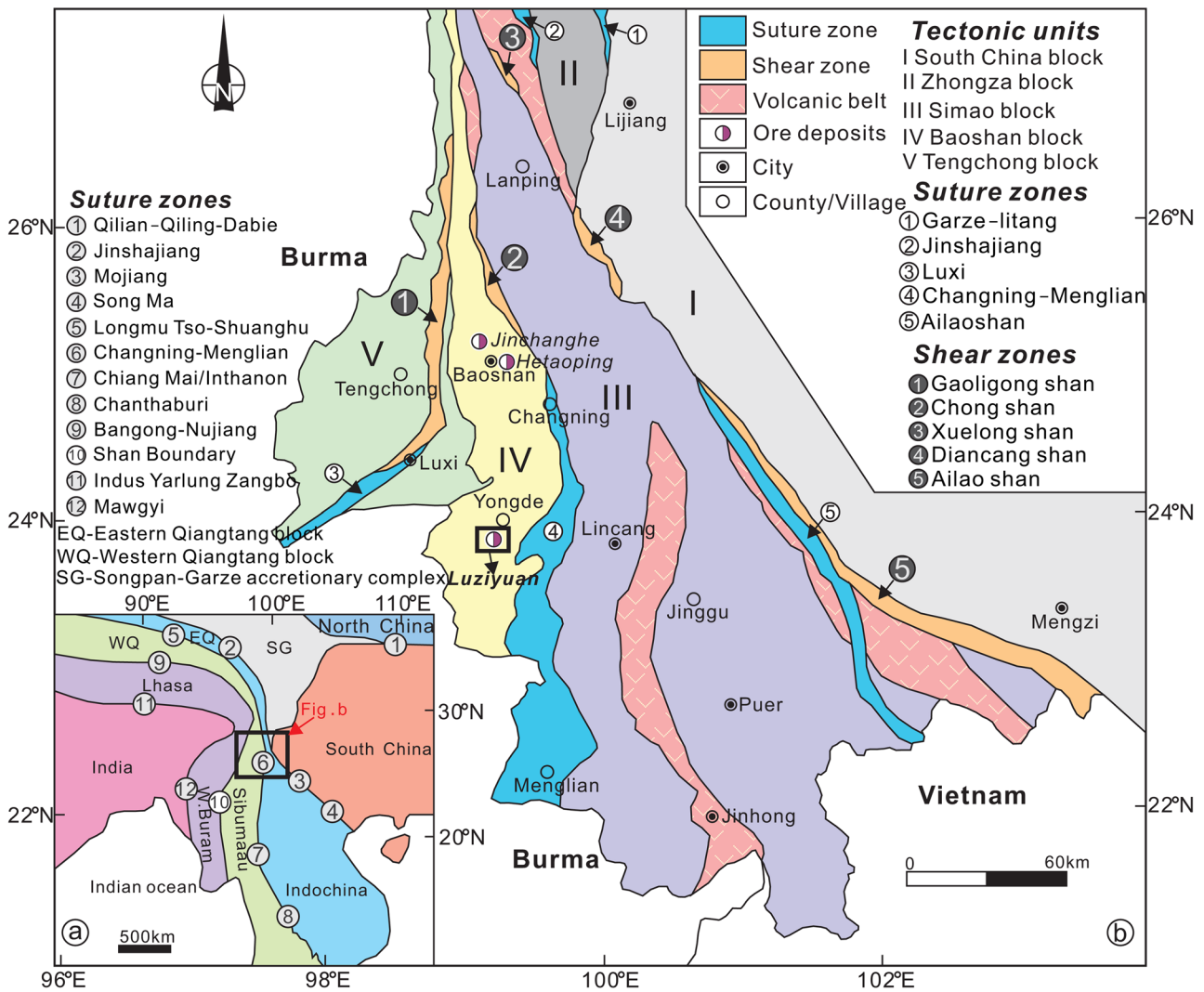
Fig. 1 a Schematic map of principal continental blocks and sutures in Southeast Asia (modified after Metcalfe 2011, 2013). **b** Tectonic framework of the southern section of the Sanjiang region showing the major continental blocks, suture zones, shear zones, volcanic belts, and location of the Luziyuan and other major Pb – Zn deposits (modified from Deng et al. 2014)

Ore deposit geology

The exposed country rock strata in the Luziyuan area include argillaceous siltstone of the Lower Ordovician Huoshaoqiao Formation, meta-siltstone of the Middle Ordovician Pupiao Formation, silty slate of the Upper Cambrian Baoshan Formation, and schist (third member), marble and quartz schist (second layer of the second member), and limestone (first layer of the second member) of the Upper Cambrian Shahechang Formation (Fig. 2a). The upper Cambrian limestones of the first layer of the second member of the Shahechang Formation are the principal host rocks to the Luziyuan Pb – Zn orebodies. No igneous bodies crop out at the surface, except for sporadic diabase dikes that follow NW–SE and NE-SW structural trends; however, geophysical exploration data indicate that a granitoid intrusion lies

concealed beneath the Luziyuan area (Li and Mo 2001; Zhao et al. 2002; Dong and Chen 2007).

The Luziyuan Pb–Zn deposit consists of three orebodies, successively numbered I, II and III from NW to SE (Fig. 2a). The main orebody (II) is stratiform to lenticular in shape, striking 051°–062°, measuring 380 – 3350 m in length and dipping 47°–61° to the northwest. It has been traced down-dip for 115–370 m (Fig. 2b). The limestone in the upper Cambrian Shahechang Formation was widely transformed to skarn. The skarn is predominantly of pyroxenoid type, and contains abundant rhodonite, actinolite, and chlorite, with subordinate garnet and diopside (Deng et al. 2013, 2016; Yang et al. 2018). These skarns are spatially zoned from the upper level to the lower level in the following sequence (Fig. 2b; Yang et al. 2018): chlorite–actinolite–calcite–quartz (1495 m above sea level, asl) → rhodonite–actinolite–fluorite–quartz–calcite (1265 m
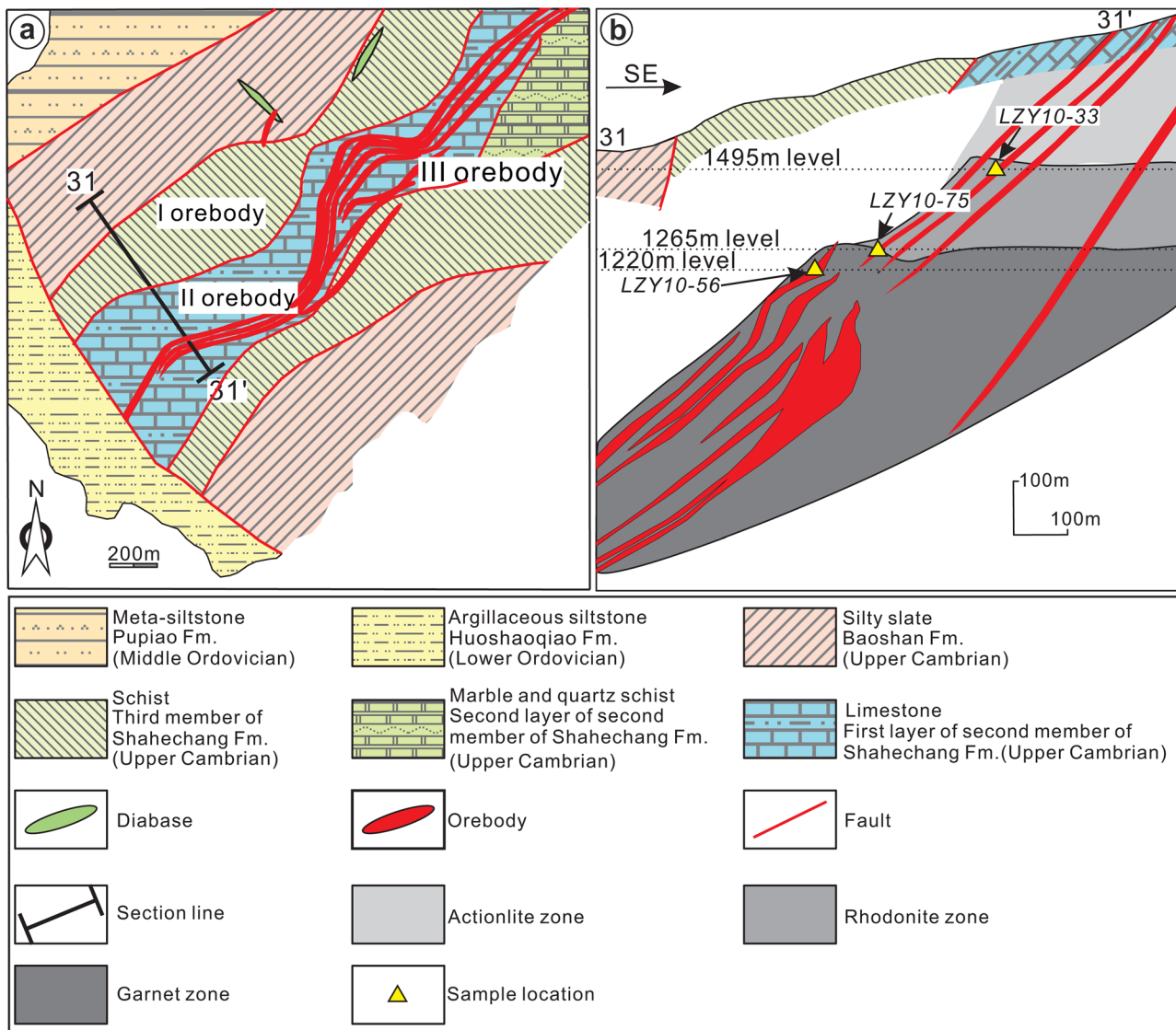
Fig. 2 **a** Geological map of the Luziyuan deposit and the distribution of orebodies. **b** The studied cross-section (line 31) through the orebodies, showing the geometry of the orebodies, vertical skarn zonation, and the sampling locations (modified from Lü et al. 2013)

asl) → garnet–rhodonite–actinolite–fluorite–quartz–calcite (1220 m asl).

The dominant ore minerals are sphalerite and galena; associated with minor pyrite and chalcopyrite. The gangue minerals are mainly rhodonite, actinolite, chlorite, quartz and calcite, along with minor garnet, diopside, and fluorite (Deng et al. 2013, 2016; Yang et al. 2018). Based on the mineral assemblages and textural relationships, mineralization at Luziyuan occurred in five stages (Yang et al. 2018): anhydrous skarn (Stage I, rhodonite + garnet + diopside), hydrous skarn (Stage II, actinolite + chlorite), early quartz (Stage III), quartz-calcite-sulfide (Stage IV, quartz + calcite + fluorite + sphalerite + galena + pyrite), and carbonate (Stage V, late quartz + calcite).

Sample materials and analytical methods

Three rhodonite containing skarn formation zones were sampled in the Luziyuan main orebody, from depths of 1495, 1265 and 1220 m asl. Double-polished petrographic thin-sections were prepared for petrographic and mineralogical studies. After initial optical petrographic assessment, locations suitable for LA-ICP-MS analysis were selected in sample areas free from scratches, containing no visible inclusions, with well-defined mineral grain boundaries. Four polished thin sections of typical rhodonite from each of the three zones were selected for in-situ LA-ICP-MS major and trace element analyses.

Mineral chemistry

The textural characteristics of rhodonite were investigated using back-scattered electron (BSE) imaging prior to LA-ICP-MS analysis. The BSE investigations were carried out using a field emission scanning electron microscope (JSM-7800F, JEOL, Japan) in combination with energy-dispersive X-ray spectrometry (TEAM Apex XL, EDAX, USA) at the State Key Laboratory of Ore Deposit Geochemistry, Institute of Geochemistry, Chinese Academy of Sciences. The imaging conditions were 25 kV voltage and 10 nA beam current. Major and trace element compositions can be analyzed precisely in situ by LA-ICP-MS without applying internal standardization by applying an ablation yield correction factor on the basis of the normalization of the sum of all metal oxides to 100 wt%, and using USGS reference glasses NIST 610, BIR-1G, BHVO-2G, BCR-2G, GSE-1G, CGSG-1, and CGSG-2 as multiple reference materials for calibration (Liu et al. 2008).

In-situ LA-ICP-MS major and trace element analyses of rhodonite were carried out using a Coherent GeoLasPro 193 nm Laser Ablation system coupled with an Agilent 7700X ICP-MS at the Guiyang Institute of Geochemistry, Chinese Academy of Sciences. Helium was applied as a carrier gas, and argon was used as the make-up gas which was mixed with the carrier gas via a T-connector before entering the plasma. A 32 μm spot diameter was adopted with a repetition rate of 4 Hz and an energy density of 1–45 J cm^{-2}. Each analysis consists of a 20-s background measurement (laser-off) followed by 40-s data acquisition. Seven standards (NIST 610, BIR-1G, BHVO-2G, BCR-2G, GSE-1G, CGSG-1, and CGSG-2) were analyzed at the beginning of the session and subsequently every set of six samples analyzed was followed by one analysis of NIST 610 as an external standard to correct laser-induced fractionation. The preferred values of element concentrations in the USGS reference glasses were taken from the GeoReM database (http://georem.mpch-mainz.gwdg.de/). Detailed analytical and data-processing methodology is described in Liu et al. (2008).

The raw ICP-MS data were treated offline using ICPMSDataCal software 10.8 and the 100%-normalization strategy (Liu et al. 2008). Selected results are presented in Supplementary Electronic Materials. The lower limits of detection (LLD) for the major and trace elements are listed in a separate column with the data (Supplementary Electronic Materials).

Sm – Nd isotope analysis

Based on field investigations and microscopic observations, several representative rhodonite and calcite samples associated with sphalerite were selected for analysis. Rhodonite
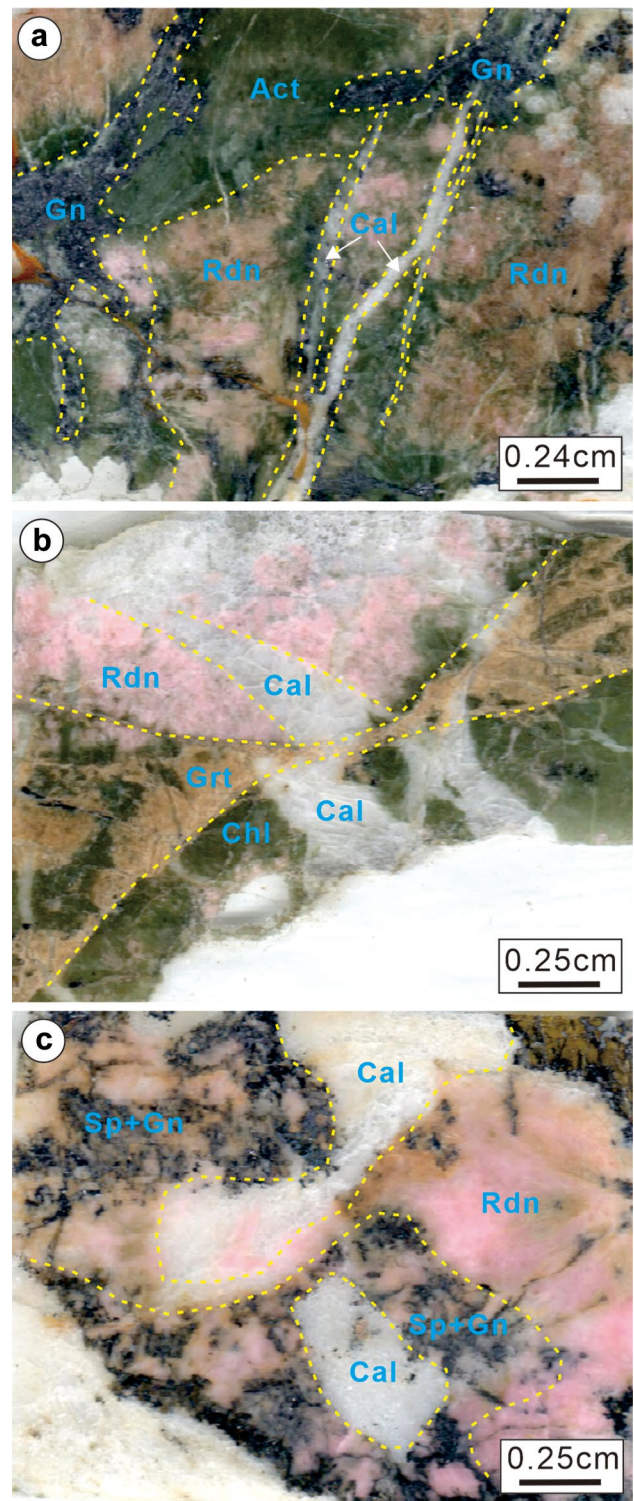

Fig. 3 Representative macroscopic features of rhodonite from three levels (1220, 1265 and 1495 m asl) in the Luziyuan deposit. **a** Sulfide-bearing coarse-grained pink rhodonite from 1220 m asl overprinted by fibrous actinolite (Act) aggregate and galena (Gn), and subsequently cut by a fine-grained calcite (Cal) vein. **b** Coarse-grained rhodonite from 1265 m asl with poor sulfide mineralization, with replacement of chlorite (Chl)-bearing garnet (Grt) skarn and crosscutting calcite vein. **c** Rhodonite from 1495 m asl showing replacement by sulfide mineralization (Sp+Gn) and calcite (Cal). Mineral abbreviations after Whitney and Evans (2010) (also for Figs. 4 and 5)

and calcite chips were cut from hand specimens and lightly crushed to a mesh size of 40–60 (250 − 400 μm), and then pure rhodonite and calcite separates were handpicked under a binocular microscope to a purity of more than 99 vol%, and finally crushed in an agate mortar to about 200 mesh size (< 75 μm).

Samples were dissolved in PTFE-lined stainless steel autoclave bombs using a mixture of concentrated HF and HClO$_4$. About 150 ± 0.1 mg of the sample was dissolved for isotope dilution, and 1000 ± 1.0 mg for isotope concentration. The abundances of Sm and Nd were determined by isotope dilution using ^{149}Sm- and ^{145}Nd-enriched spikes. Present-day ^{143}Nd/^{144}Nd ratios were determined from unspiked solutions of pre-concentrated samples. Sm and Nd were separated by a reversed-phase extraction technique with HDEHP to avoid interference of ^{144}Sm with ^{144}Nd.

The Sm and Nd abundances and isotopic ratios were measured using a Triton thermal-ionization mass-spectrometer (TIMS) at the Tianjin Institute of Geology and Mineral Resources, Chinese Academy of Geological Sciences. Nd isotopic ratios were normalized to ^{146}Nd/^{144}Nd = 0.7219 using a power law fractionation correction. Concentrations for BCR-1 determined during this study were 6.571 ppm Sm, 8.753 ppm Nd, and the ^{143}Nd/^{144}Nd value was 0.512644 ± 5. The JMC standard provided a ^{143}Nd/^{144}Nd value of 0.511132 ± 5. Blanks during the course of this study measured 30 pg Sm and 54 pg Nd. The precision of the Sm and Nd concentrations at the two-sigma level (2σ) was less than 0.5% of the quoted values, and the analytical error (2σ) of ^{147}Sm/^{144}Nd was $\pm 0.5\%$. The Sm − Nd isochron age was calculated using the ISOPLOT program (Ludwig 2003).
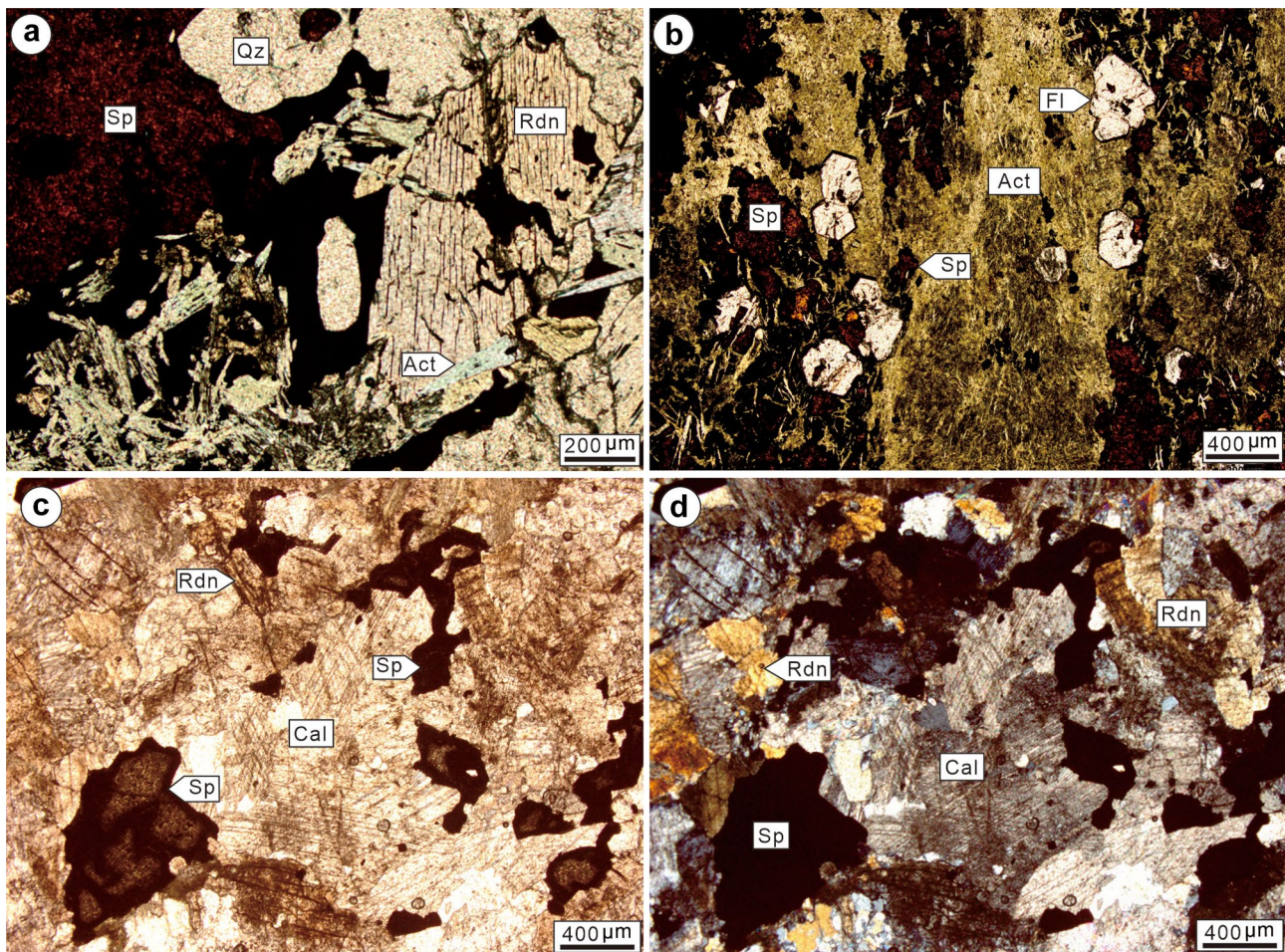

Fig. 4 Representative photomicrographs of rhodonite shown in Fig. 3. **a** Replacement of rhodonite (Rdn) by fibrous actinolite (Act) and sphalerite (Sp) along the rim; plane-polarized light. **b** Sphalerite (Sp) grains are coexisted with fibrous actinolite (Act) and euhedral fluorite (Fl); plane-polarized light. **c** Subhedral rhodonite replaced by anhedral sphalerite along cleavage planes and then by calcite (Cal); plane-polarized light. **d** The same area as in **c** observed in cross-polarized light
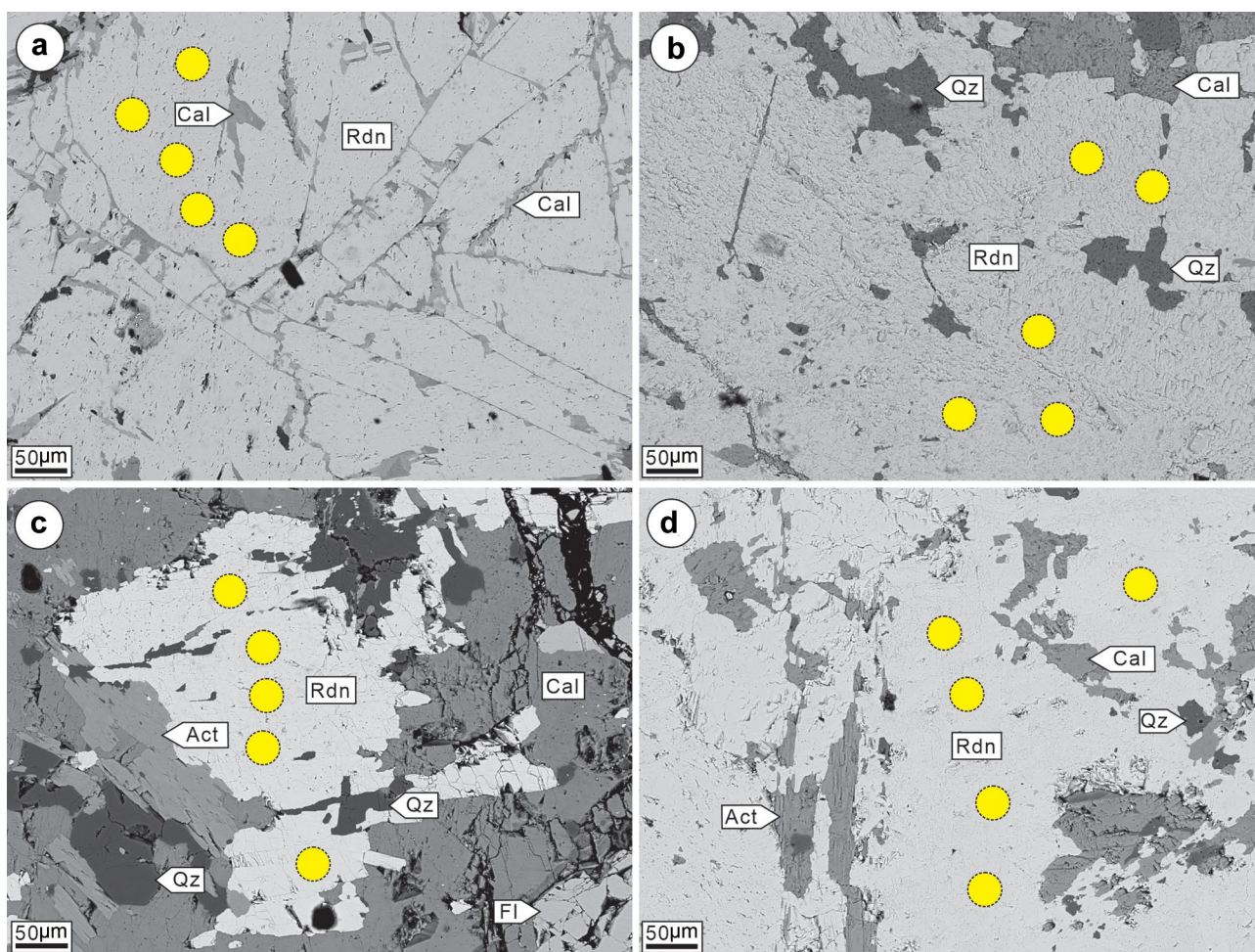
Fig. 5 BSE images of rhodonite from the Luziyuan Pb–Zn skarn deposit. **a-b** Veinlets of calcite and quartz along fractures in rhodonite. **c-d** Fibrous aggregates of actinolite together with calcite, quartz and fluorite replacing rhodonite along its margin. Yellow circles show the location of LA–ICP–MS spot analyses. Abbreviations: Rdn–rhodonite, Cal–calcite, Qz–quartz, Act–actinolite, Fl–fluorite

Results

Rhodonite petrography

Pyroxene skarns (clinopyroxene > garnet) are predominant in three zones of the Luziyuan deposit. These zones, where pyroxene skarns are the dominant skarn type, are considered a distal metasomatic system (Meinert et al. 2005). In the Luziyuan ore area, on a centimeter to meter scale it is possible to recognize patches of pink prismatic rhodonite crystals associated with sulfides (e.g., sphalerite and galena) replacing marble (Fig. 3). Based on observations from hand

Table 1 Sm − Nd isotope analyses of rhodonite and calcite from the Luziyuan district

Sample no.	Mineral	Sm/ppm	Nd/ppm	$^{147}Sm/^{144}Nd$	2σ	$^{143}Nd/^{144}Nd$	2σ
LZY10-16	Calcite	0.789	4.112	0.1160	0.0005	0.511820	0.000012
LZY10-54	Calcite	1.389	4.852	0.1730	0.0005	0.511888	0.000009
LZY10-45	Calcite	3.520	15.342	0.1387	0.0005	0.511847	0.000017
LZY10-51	Calcite	1.870	7.290	0.1551	0.0005	0.511865	0.000015
LZY10-40	Calcite	1.100	2.884	0.2305	0.0005	0.511959	0.000012
LZY10-18	Calcite	1.180	5.693	0.1253	0.0005	0.511834	0.00003
LZY10-71	Calcite	0.507	1.922	0.1596	0.0005	0.511872	0.000023
LZY10-69	Rhodonite	0.150	0.297	0.3059	0.0005	0.512039	0.000026
LZY10-58	Rhodonite	0.666	0.988	0.4074	0.0005	0.512171	0.000006

specimens, rhodonite at level 1220 m asl is present as relict grains partially replaced by abundant sulfide mineralization, fibrous actinolite and calcite (Fig. 3a). Rhodonite from level 1265 m asl occurs as coarse-grained crystals with minor sulfide mineralization replacing earlier garnet and cut by calcite veins (Fig. 3b). Rhodonite from shallow levels within deposit (1495 m asl) is replaced by abundant sulfide mineralization and calcite (Fig. 3c). In thin section, this rhodonite occurs as subhedral crystals with first-order interference colors and is partially replaced by actinolite and sphalerite along cleavage planes (Fig. 4a − d).

In BSE images, most rhodonite grains are subhedral to anhedral columnar, range 0.4–1 mm in size and devoid of compositional zoning (Fig. 5a–d). Associated minerals include actinolite, calcite, quartz, and fluorite. Abundant calcite and minor quartz occur as veinlets or fine-grained anhedral crystals along cleavage planes or fractures within rhodonite crystals (Fig. 5a–d). Actinolite occurs as fibrous aggregates associated with minor fluorite and replaces precursor rhodonite along the grain margins (Fig. 5c).

Sm − Nd geochronology

The results of the Sm − Nd isotope analysis are presented in Table 1 and the Sm − Nd isochron diagram (Fig. 6). The Sm and Nd concentrations within the measured samples varied by almost an order of magnitude (Table 1). Variations in $^{147}Sm/^{144}Nd$ ratio were large, ranging from 0.12 to 0.41. Nine samples yielded an age of 183 ± 2.3 Ma and an initial $^{143}Nd/^{144}Nd$ ratio of 0.5117. The ISOPLOT program (Ludwig 2003) gave a mean squared weighted deviation (MSWD) of
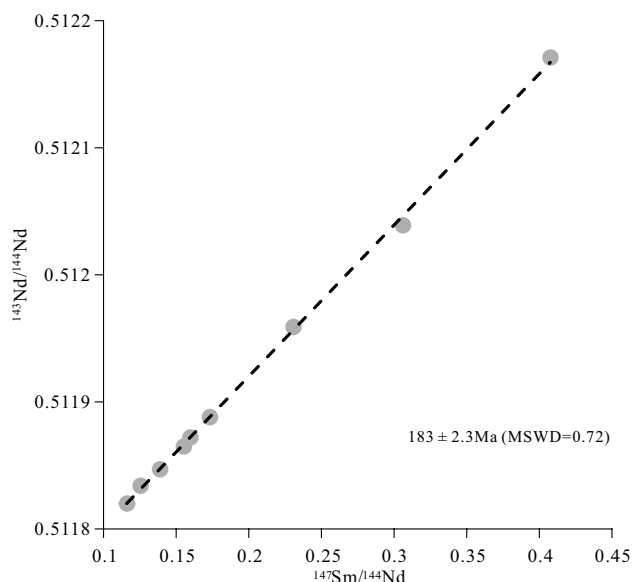

Fig. 6 Sm − Nd isochron diagram for the rhodonite − calcite pair from the Luziyuan district

0.72. The extremely low MSWD indicates that non-analytical scatter of initial $^{143}Nd/^{144}Nd$ ratios is limited (Chesley et al. 1994). Therefore, the spread in the $^{147}Sm/^{144}Nd$ ratios and consistency of the initial $^{143}Nd/^{144}Nd$ ratios indicate that the age obtained in this study is reliable.

Major element composition of rhodonite

Major element contents in rhodonite from three levels (1495, 1265 and 1220 m asl) in the Luziyuan orebody were analyzed by LA-ICP-MS. Selected analyses are collated in Table 2, the compositional variation of these rhodonite samples is presented in the ternary Mn-Ca-(Fe + Mg) diagram (Fig. 7). Additional compositional data are given in the Supplementary Electronic Materials.

The LA-ICP-MS data show that all rhodonite samples from in the Luziyuan are dominated by MnO (34.7 − 43.0 wt%) with minor amounts of FeO (1.07 − 6.80 wt%) and MgO (0.42 − 2.54 wt%; Table 2 and Fig. 7). The variation of Mn and Fe contents in rhodonite is considerable. In terms of pyroxenoid end-member compositions, the variations amount to 62 − 77 mol% $MnSiO_3$, 16 − 21 mol% $CaSiO_3$ and 4–18 mol% $(Fe, Mg)SiO_3$ (Fig. 7). The $MnSiO_3$ content of rhodonite increases from 1220 m asl to 1495 m asl and all measured compositions fall in the rhodonite field (Fig. 7). We have compiled data for major element compositions of rhodonites from other Pb − Zn skarn deposits including the Monte Civillina Pb − Zn deposit in Italy (Abrecht 1985) and the Groundhog Pb − Zn deposit in New Mexico (Meinert 1987), which reveal that these skarn pyroxenoids are dominated by rhodonite.

Rare earth and trace element composition of rhodonite

The rare earth and trace element contents were analyzed by LA-ICP-MS; data are included with Table 3 and the Supplementary Electronic Materials. Most analyzed samples have extremely low REE concentrations (< 1 ppm), but well above the minimum detection limit (0.03 ppm for Pr − 0.37 ppm for Nd) (Table 3). Their REE patterns and chondrite-normalized diagrams cannot be used to discuss the nature of fluid responsible for rhodonite formation. However, we used major (Fe and Mn) and trace elements (Zn, Y and Ho) to interpret the causes of Zn mineralization. Data for all rhodonites show strong positive correlation between Y and Ho (Fig. 8).

All rhodonite samples from three levels have high levels of Zn (536–2117 ppm) and relatively low Co (0.4 − 11.8 ppm), Ni (up to 5.0 ppm), Cu (up to 4.4 ppm), Ga (0.4 − 3.6 ppm), Mo (2.0 − 3.9 ppm), Sn (up to 2.5 ppm), W (up to 1.2 ppm) and variable Pb (0.3 − 23.8 ppm) contents (Table 3). The trace element abundances normalized to the bulk continental

Table 2 Selected major element (wt%) contents by LA-ICP-MS, in rhodonite from the Luziyuan deposit

Sample no	LLD	LZY10 33-4-2	LZY10 33-3-2	LZY10 33-1-1	LZY10 33-2-1	LZY10 75-1	LZY10 75-3	LZY10 75-5	LZY10 75-7	LZY10 58-4	LZY10 58-7	LZY10 58-8	LZY10 69-4	LZY10 71-6	LZY10 71-7	LZY10 71-9	LZY10 71-11
Description		rhodonite and calctie-bearing sulfide ore				rhodonite skarn with calcite vein				rhodonite-bearing sulfide ore				chalcopyrite and sphalerite-bearing rhodonite skarn			
level		1495 m asl				1265 m asl				1220 m asl							
Na_2O	0.002	0.006	0.008	0.017	0.011	0.014	0.009	0.023	0.013	0.009	0.008	0.013	0.006	0.004	0.004	0.010	0.006
MgO	0.0006	1.00	0.49	0.56	0.57	1.00	0.94	1.46	0.79	0.82	0.84	0.85	0.74	0.74	0.63	0.73	0.68
Al_2O_3	0.0003	0.007	0.005	0.016	0.020	0.010	0.012	0.017	0.003	0.006	0.009	0.009	0.018	0.003	0.003	0.006	0.004
SiO_2	0.05	46.2	46.1	46.2	46.5	46.8	46.5	46.8	46.5	46.0	46.2	46.1	45.3	45.8	45.7	46.1	46.2
P_2O_5	0.01	0.009	0.012	0.001	0.000	0.002	0.007	0.005	0.010	0.003	0.001	0.004	0.004	0.005	0.002	0.007	0.002
K_2O	0.002	0.002	0.002	0.009	0.005	0.006	0.005	0.010	0.004	0.004	0.003	0.005	0.006	0.002	0.002	0.003	0.003
CaO	0.05	9.24	9.19	9.04	8.59	7.45	7.39	7.98	7.03	7.37	8.15	8.00	8.00	8.47	8.34	8.26	7.75
TiO_2	0.0003	0.0008	0.0002	0.0006	0.002	0.0002	0.0006	0.0009	0.0004	0.0008	0.0005	0.0006	0.0003	0.0003	0.0003	0.0002	0.0001
MnO	0.0004	41.4	42.6	42.8	43.0	39.4	40.0	38.3	40.8	41.6	39.9	41.2	39.5	40.8	42.0	40.6	41.6
FeO	0.004	1.97	1.40	1.07	1.17	4.84	4.67	4.94	4.32	3.86	4.58	3.56	5.97	3.70	2.99	3.80	3.36
total		99.8	99.9	99.8	99.8	99.5	99.6	99.5	99.6	99.7	99.6	99.7	99.5	99.6	99.6	99.6	99.6
Number of ions on the basis of 15O																	
Na		0.001	0.002	0.004	0.002	0.003	0.002	0.005	0.003	0.002	0.002	0.003	0.001	0.001	0.001	0.002	0.001
Mg		0.161	0.079	0.090	0.092	0.160	0.151	0.233	0.126	0.132	0.134	0.136	0.121	0.120	0.102	0.118	0.110
Al		0.001	0.001	0.002	0.003	0.001	0.002	0.002	0.000	0.001	0.001	0.001	0.002	0.000	0.000	0.001	0.001
Si		4.934	4.940	4.948	4.967	4.999	4.982	4.985	4.988	4.947	4.951	4.943	4.898	4.927	4.924	4.953	4.957
P		0.001	0.001	0.000	0.000	0.000	0.001	0.000	0.001	0.000	0.000	0.000	0.000	0.000	0.000	0.001	0.000
K		0.000	0.000	0.001	0.001	0.001	0.001	0.001	0.001	0.001	0.000	0.001	0.001	0.000	0.000	0.000	0.000
Ca		1.057	1.055	1.037	0.984	0.853	0.847	0.910	0.808	0.849	0.937	0.920	0.928	0.977	0.962	0.950	0.892
Ti		0.000	0.000	0.000	0.000	0.000	0.000	0.000	0.000	0.000	0.000	0.000	0.000	0.000	0.000	0.000	0.000
Mn		3.735	3.856	3.875	3.881	3.555	3.616	3.440	3.699	3.776	3.615	3.735	3.613	3.715	3.818	3.683	3.781
Fe		0.175	0.125	0.096	0.104	0.431	0.416	0.438	0.386	0.345	0.409	0.319	0.539	0.332	0.269	0.340	0.301
$MnSiO_3$		0.73	0.75	0.76	0.77	0.71	0.72	0.69	0.74	0.74	0.71	0.73	0.69	0.72	0.74	0.72	0.74
$CaSiO_3$		0.21	0.21	0.20	0.19	0.17	0.17	0.18	0.16	0.17	0.18	0.18	0.18	0.19	0.19	0.19	0.18
$(Fe,Mg)SiO_3$		0.07	0.04	0.04	0.04	0.12	0.11	0.13	0.10	0.09	0.11	0.09	0.13	0.09	0.07	0.09	0.08

LLD lower limits of detection

Fig. 7 Triangular plot of ferrosilite (Fe, Mg)SiO₃, wollastonite (CaSiO₃) and rhodonite (MnSiO₃) molecular proportions in rhodonite from the Luziyuan Pb−Zn deposit. The data for the Monte Civillina and Groundhog Pb−Zn deposits are taken from Abrecht (1985) and Meinert (1987). Pyroxenoid miscibility gap is shown by dashed lines (from Abrecht and Peters 1980)
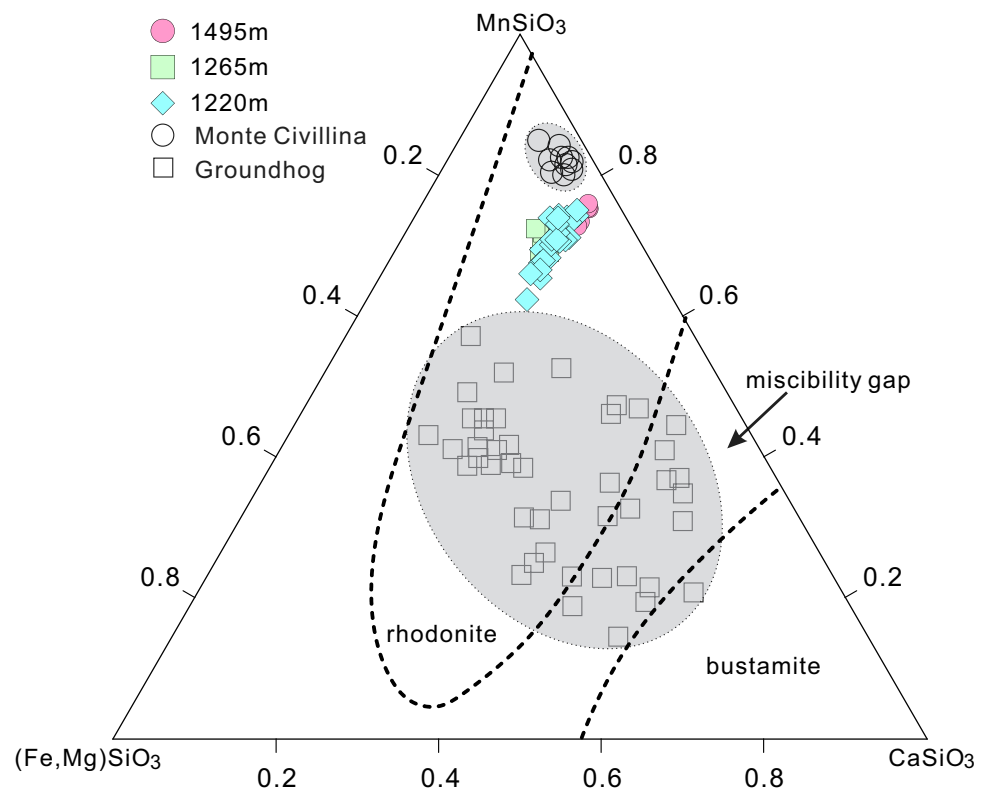
crust (Fig. 9) show strong Zn enrichment and slight Mo enrichment; samples from 1265 m asl and 1220 m asl have significant depletion of Co, Ni, Cu, Ga, Sn and W.

Discussion

Geological significance of Sm−Nd dating of rhodonite−calcite pair

Sm−Nd geochronology of Ca-bearing minerals (e.g., calcite, fluorite, and garnet) is a promising dating tool for hydrothermal systems, due to the isomorphous substitution of REE for Ca^{2+}, intense fractionation of REE in hydrothermal systems, and strong resistance of weathering (Morgan and Wandless 1980; McCulloch and Compston 1981; Pan and Fleet 1996). This technique has been applied to constrain the timing of the formation of some hydrothermal deposits (e.g., fluorite dating of Mississippi Valley-type deposits, Chesley et al. 1994; calcite dating of Shuiyindong Carlin-type gold deposit, Su et al. 2009; scheelite dating of Muruntau Au(-W) deposit, Kempe et al. 2001). Published ages of the Pb−Zn deposits in the Baoshan-Zhenkang block are very few (e.g., 116±3.9 Ma Hetaoping deposit, Tao et al. 2010; 142±2.6 Ma Luziyuan deposit, Zhu et al. 2011; 117−120 Ma Jinchanghe deposit, Huang et al. 2014). These measurements are based on the Rb−Sr isotopic compositions of sulfide assemblages (e.g.,

sphalerite, pyrite, and chalcopyrite), but the reliability of Rb−Sr dating in these systems remains doubtful due to uncertainties regarding the cause of Rb−Sr fractionation and the exact host of Rb and Sr in these mineral assemblages (Halliday et al. 1991). Some researchers (Christensen et al. 1995; Bradley et al. 2004) have noted that inclusions of carbonate or silicate, or primary or secondary fluid inclusions in sphalerite could impart differing $^{87}Sr/^{86}Sr$ ratios, resulting in ambiguous dating results.

Recently, a Sm–Nd geochronological study has been carried out on calcite from the Luziyuan deposit and suggested that Pb–Zn skarn mineralization was formed in the Early Cretaceous (130±15 Ma) (Xu et al. 2020). Unfortunately, this value was only based on just four calcite samples syngenetic with the mineralization and has relatively large uncertainties. The present contribution provides new rhodonite−calcite Sm−Nd isotopic data, which yield the first reliable age determination for Pb−Zn deposits in the Baoshan block. The data for all of the studied samples define an isochron line yielding an age of 183 Ma (Fig. 6), suggesting that the Luziyuan Pb−Zn mineralization formed in the Early Jurassic. There is no evidence of granitoid magmatism in the Luziyuan area; only the Muchang A-type granite intrusion with an age of 266 Ma (Ye et al. 2010) crops out 14 km southeast of Luziyuan. The new rhodonite Sm−Nd age (183 Ma) is obviously younger than the age of the Muchang granite, although it was previous suggested

Table 3 Selected trace element (ppm) contents by LA-ICP-MS, in rhodonite from the Luziyuan deposit

| Sample no	LLD	LZY10 33-4-2	LZY10 33-3-2	LZY10 33-1-1	LZY10 33-2-1	LZY10 75-1	LZY10 75-3	LZY10 75-5	LZY10 75-7	LZY10 58-4	LZY10 58-7	LZY10 58-8	LZY10 69-4	LZY10 71-6	LZY10 71-7	LZY10 71-9	LZY10 71-11
Description		rhodonite and calcite-bearing sulfide ore				rhodonite skarn with calcite vein				rhodonite-bearing sulfide ore				chalcopyrite and sphalerite-bearing rhodonite skarn			
level		1495 m asl				1265 m asl				1220 m asl							
Co	0.10	0.72	0.45	0.51	0.42	5.07	4.84	6.16	4.38	2.85	4.07	2.17	5.46	2.80	2.18	3.20	2.44
Ni	0.95	1.02	0.17	0.26	0.07	0.59	0.23	0.86	0.53	0.59	0.37	0.00	0.68	0.72	0.11	0.00	0.19
Cu	1.07	0.33	0.00	1.58	2.27	1.45	0.20	0.00	0.00	0.07	0.00	0.13	1.52	0.46	0.00	0.21	0.00
Zn	2.45	1311	859	651	654	1975	1772	1891	1758	918	1347	818	1660	2005	1422	1969	1732
Ga	0.35	3.47	3.08	1.00	1.15	0.70	0.84	0.43	0.59	0.91	0.62	1.00	0.79	0.57	0.62	0.67	0.91
Mo	0.40	1.97	2.18	3.68	3.59	3.55	3.16	3.24	3.04	3.45	2.98	3.32	2.64	3.44	3.00	2.92	2.76
Sn	0.28	1.75	1.60	0.71	1.26	0.13	0.00	0.00	0.06	0.01	0.14	0.08	0.13	0.23	0.20	0.29	0.13
W	0.24	1.16	0.20	0.14	0.08	0.26	0.23	0.08	0.21	0.12	0.16	0.12	0.20	0.58	0.26	0.33	0.10
Pb	0.12	6.32	9.52	1.14	1.17	17.7	6.53	14.7	20.3	0.38	0.43	0.61	2.66	0.44	0.59	1.01	0.70
La	0.05	0.35	0.22	0.48	0.32	0.12	0.12	0.10	0.07	0.05	0.05	0.10	0.07	0.19	0.16	0.32	0.15
Ce	0.06	0.71	1.10	1.99	2.24	0.27	0.23	0.19	0.23	0.12	0.22	0.39	0.08	0.33	0.29	0.43	0.28
Pr	0.03	0.15	0.23	0.39	0.45	0.06	0.03	0.03	0.05	0.01	0.06	0.10	0.01	0.07	0.04	0.06	0.06
Nd	0.37	0.80	1.10	2.70	4.22	0.35	0.12	0.34	0.26	0.25	0.66	1.22	0.34	0.55	0.40	0.33	0.40
Sm	0.34	0.40	0.76	0.78	1.21	0.09	0.05	0.17	0.29	0.33	0.31	0.32	0.33	0.08	0.08	0.23	0.21
Eu	0.08	0.12	0.32	0.16	0.22	0.04	0.02	0.02	0.05	0.08	0.03	0.08	0.03	0.07	0.05	0.07	0.09
Gd	0.23	0.35	0.62	0.97	1.01	0.04	0.16	0.13	0.16	0.19	0.03	0.19	0.08	0.09	0.18	0.00	0.25
Tb	0.04	0.07	0.12	0.10	0.21	0.02	0.01	0.03	0.01	0.03	0.00	0.05	0.00	0.01	0.03	0.03	0.05
Dy	0.16	0.59	0.82	0.66	1.10	0.17	0.00	0.13	0.07	0.14	0.11	0.17	0.22	0.04	0.13	0.08	0.25
Ho	0.05	0.09	0.11	0.11	0.18	0.02	0.00	0.02	0.01	0.01	0.00	0.02	0.00	0.02	0.03	0.02	0.06
Er	0.14	0.22	0.21	0.17	0.37	0.08	0.05	0.16	0.03	0.10	0.00	0.02	0.09	0.15	0.15	0.11	0.08
Tm	0.04	0.03	0.03	0.00	0.02	0.04	0.00	0.04	0.02	0.00	0.01	0.00	0.02	0.01	0.01	0.00	0.04
Yb	0.23	0.08	0.03	0.02	0.32	0.17	0.10	0.28	0.06	0.08	0.02	0.00	0.24	0.26	0.15	0.12	0.15
Lu	0.05	0.02	0.00	0.00	0.00	0.08	0.04	0.04	0.05	0.00	0.02	0.01	0.04	0.01	0.03	0.02	0.04
Y	0.04	3.40	5.78	3.75	5.63	0.54	0.41	0.99	0.40	0.86	0.36	0.63	0.50	0.63	0.93	0.57	1.67
U	0.06	1.02	0.36	0.45	0.63	0.16	0.11	0.11	0.11	0.08	0.14	0.07	0.09	0.18	0.13	0.34	0.09
Mn/Fe		20.9	30.4	39.8	36.7	8.11	8.53	7.71	9.41	10.7	8.67	11.5	6.59	11.0	14.0	10.6	12.3
ΣREE		4.00	5.68	8.53	11.9	1.53	0.93	1.69	1.35	1.39	1.50	2.68	1.56	1.89	1.74	1.84	2.11
δEu		0.32	0.47	0.19	0.20	0.60	0.12	0.14	0.22	0.30	0.15	0.32	0.14	0.87	0.36	0.60	0.41

LLD lower limits of detection
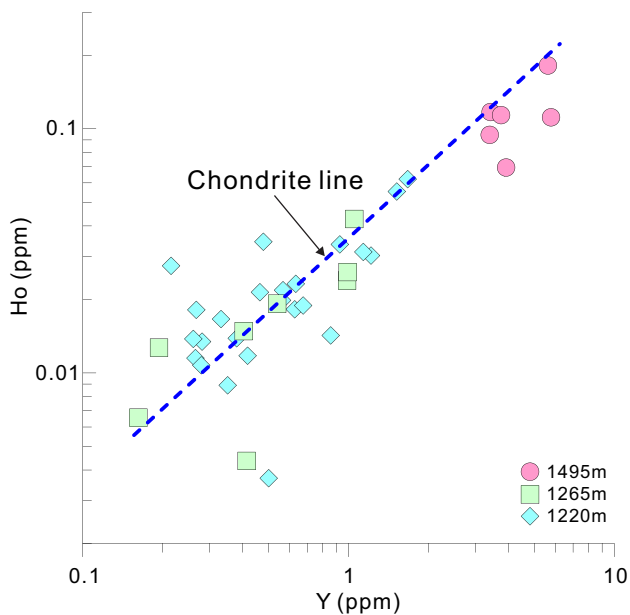
Fig. 8 Diagram of Y versus Ho in rhodonite. Chondrite line is from Anders and Grevesse (1989)

that the Luziyuan deposit is linked to the Muchang granite (Zhao et al. 2002; Dong and Chen 2007; Ye et al. 2010). Published geophysical data (Li and Mo 2001) suggest that there are unexposed intermediate-acidic intrusive rocks

underlying the ore district. The geophysically detected intrusion is hypothesized to be related to the Muchang granite and associated with the Pb − Zn mineralization (Zhao et al. 2002; Dong and Chen 2007). Furthermore, the Luziyuan skarn is characterized by distinctive Mn enrichment (e.g., the presence of rhodonite). Its Mn/Fe ratios (5.5 − 39.8, Table 3) are much higher than those of clinopyroxenes (Mn/Fe < 0.1, Nakano et al. 1994) in Cu–Fe skarn deposits at or close to intrusion contacts, which suggests that Luziyuan is a distal skarn deposit lacking conspicuous evidence of igneous activity in its vicinity (Meinert et al. 2005). Therefore, the distal rhodonite occurrence in this area can be used to indicate the existence of non-exposed intrusion in the district and a possible link between the Luziyuan deposit and the hidden granitoid intrusion.

Interpretation of the tectonic setting of Pb − Zn metallogenic systems in the Baoshan-Zhenkang block remains unclear due to a lack of reliable age constraints for mineralization. As mentioned above, we hypothesize that both the Luziyuan mineralization and the surmised intrusion were formed during the Indochina epoch. Based on the evolution model of tectonics, magmatism and metallogeny in the Sanjiang region proposed by Deng et al. (2014), the Luziyuan Pb − Zn metallogenic processes and associated magmatism could be related to the eastward subduction of the Shan Boundary Ocean toward the Tengchong-Baoshan

Fig. 9 Trace element abundances in the Luziyuan rhodonite normalized to the bulk continental crust; normalization values are from Rudnick and Gao (2003)
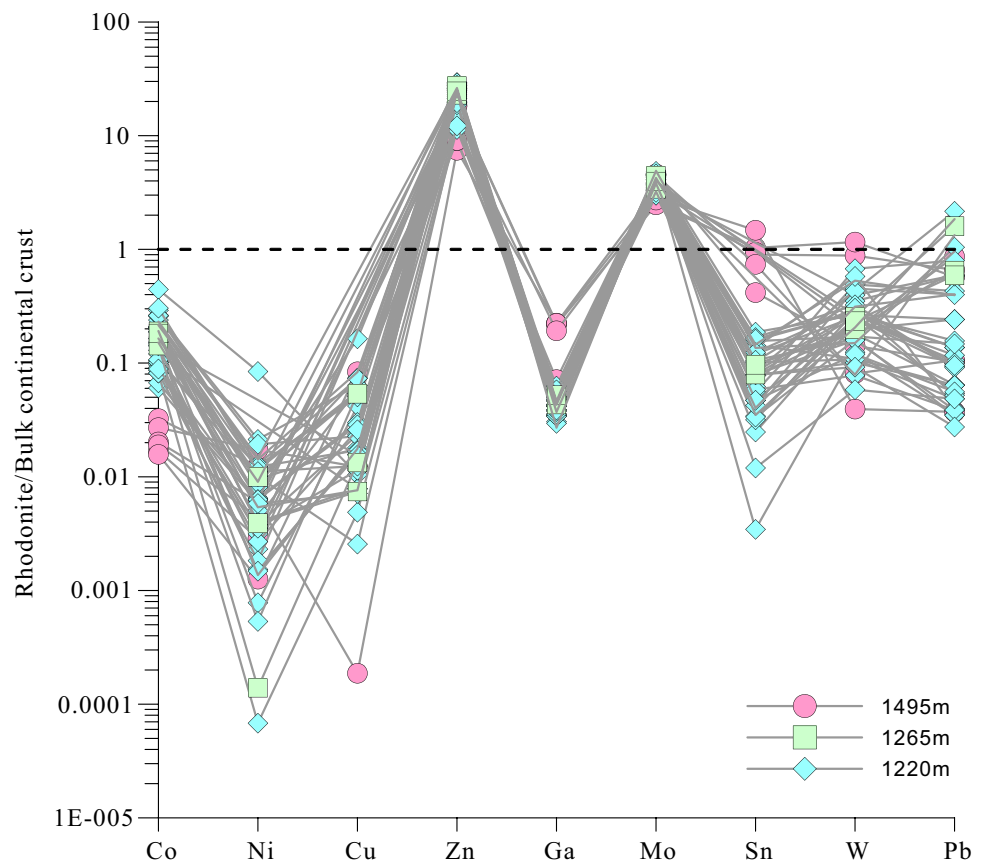
block, rather than the eastward subduction of Nujiang Ocean toward the West Qiangtang block during the Meso-Tethys period. If the concealed intrusion is genetically related to the Muchang A-type granite (Dong and Chen 2007; Ye et al. 2010), the Luziyuan deposit was formed in a continental extensional setting in response to subduction of the Shan Boundary Ocean.

Implications for rhodonite formation

As shown in Fig. 9, all rhodonite samples from the Luziyuan area are enriched in Zn (536 − 2117 ppm) and slightly enriched in Mo (2.0 − 3.9 ppm). Factors that control the mineralogy of skarn systems include extrinsic mechanisms (e.g., changes in P, T, X of the fluid) and intrinsic mechanisms (e.g., surface adsorption, mineral diffusion, and growth rate) (Gaspar et al. 2008), and the influence of Mn or Fe contents in rhodonites on Zn enrichment will be examined in this study.

The relationships between the Zn, Mn and Fe contents in clinopyroxenes from typical Cu − Fe and Pb − Zn skarn deposits have been evaluated by Nakano et al. (1994). As shown in Fig. 10, clinopyroxenes from Cu − Fe skarn deposits have low Zn and Mn contents, but high Fe contents. In contrast, Pb − Zn skarn deposits contain clinopyroxenes with relatively high contents of Zn and Mn, but relatively low Fe contents. This slightly positive correlation between Zn and Mn in clinopyroxene may imply that Zn enrichment could be controlled by Mn contents in the fluid. The rhodonite from the Luziyuan deposit has high Zn and Mn contents, and extremely low Fe contents in comparison with the data for clinopyroxene in Pb − Zn skarn deposits reported by Nakano et al. (1994) (Fig. 10). As indicated by Shannon (1976), the ionic radius of Zn is closer to the ionic radius of Fe^{2+}, rather than Mn^{2+} and, hence, the fluid had to have a high Mn/Fe ratio. Therefore, it is likely that the Zn enrichment at Luziyuan owes to extreme Mn enrichment of the mineralizing fluid relative to Fe. In skarn systems, the general compositional evolution of clinopyroxene-forming fluid is: depletion first in Mg, then in Fe, and finally in Mn (Burt 1977). This sequence suggests that Mn is transported the farthest from the source, compared to Mg or Fe and that the Mn/Fe ratio of the clinopyroxene-forming fluid increased gradually with fluid evolution. Noticeably, the ore-forming chalcophile elements (e.g., Cu, Fe, Pb, and Zn) also show a similar variation in skarn-producing fluids: first depletion in Cu + Fe and then in Zn + Pb (Meinert et al. 2003). Therefore, we infer that the parental Mn-rich fluid could also be enriched in Zn and Pb. In general, Zn or Pb are typically derived from sedimentary rocks (Xu 2016), whereas Mn may originate from sedimentary rocks or magma. In the Luziyuan Pb − Zn deposit, the host carbonate rocks are characterized by extremely low MnO contents (0.08 − 0.29 wt%; Wang 2016); thus, it is
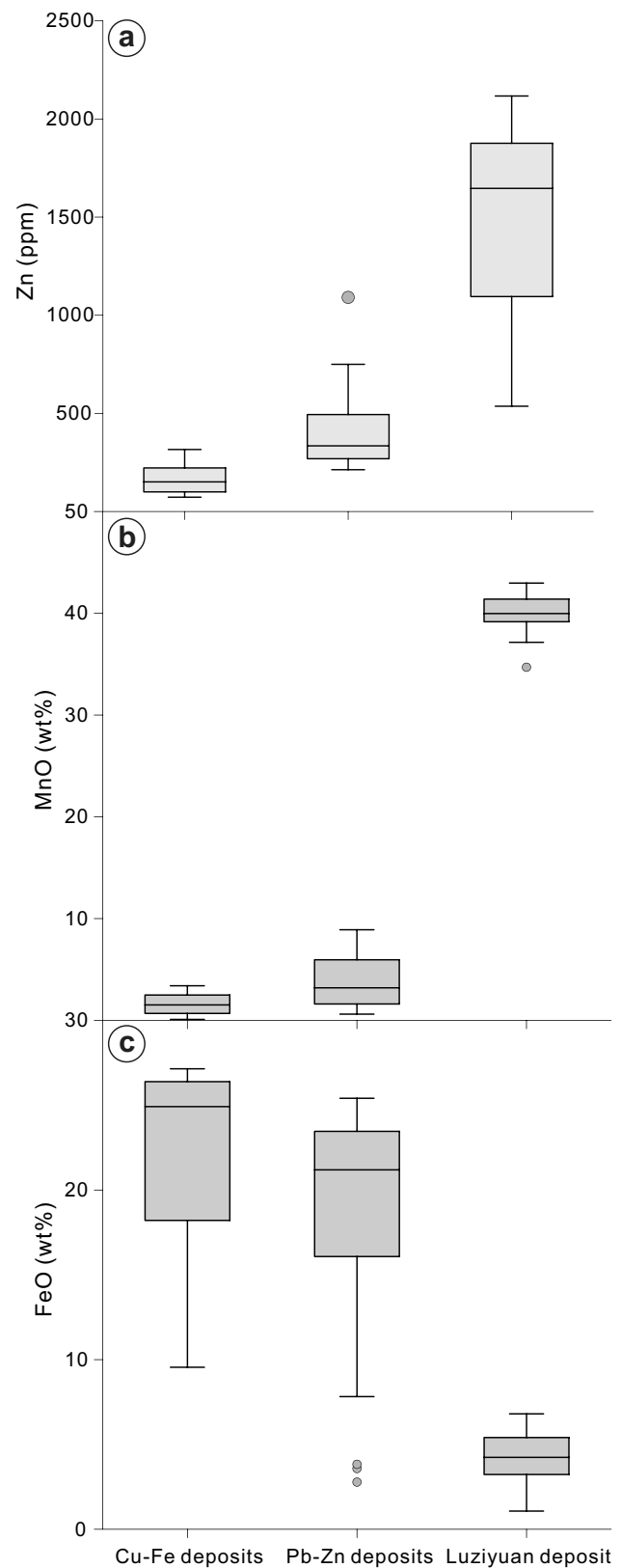

Fig. 10 Box plots of the Zn concentrations **a**, MnO **b** and FeO **c** contents in rhodonite from Luziyuan. The data for other Cu − Fe and Pb − Zn skarn deposits are taken from Nakano et al. (1994)

unlikely that Mn was mainly derived from the host rock. The possibility of different fluid sources can be addressed using the Y and Ho contents of rhodonite from the Luziyuan deposit. These elements are similar because they are trivalent and have comparable ionic radii (Shannon 1976). This geochemical twin pair remains coupled during geochemical processes, resulting in a consistent, chondritic Y/Ho atomic weight ratio of 28 for most igneous rocks (Anders and Grevesse 1989; Bau 1996). The Luziyuan rhodonite from different levels also shows chondritic Y/Ho ratios (Fig. 8), which indicates that the Mn-rich hydrothermal fluids were probably derived from a magmatic source. Therefore, our interpretation of Zn-rich rhodonite in the study area is that a Mn-bearing magmatic-hydrothermal fluid was enriched in Zn through interaction with the basement rocks and then formed the rhodonite by reacting with the limestone. Although there is much uncertainty in factors such as temperature and sulfur species in the fluid, it is probable that the incorporation of Zn into rhodonite can more readily take place when the Mn-rich hydrothermal fluid contains elevated concentrations of Zn. Previous studies have shown that skarn deposits generally follow a zoned mineralization pattern (e.g., $Fe-Mo \rightarrow Fe-Sn \rightarrow Sn-W-Cu \rightarrow Cu-Zn \rightarrow Zn-Pb-Ag$) from the contact zone of igneous rocks into carbonate wall rocks (Zhao 1997; Zhao et al. 2002). In this zoning sequence, Fe, Mo, Sn and Cu mineralization is confined to magnesian or calcic skarns, whereas $Pb-Zn-Ag$ mineralization is invariably associated with manganoan skarns. These workers suggested that manganoan skarns can be used as the most important exploration indicator for $Pb-Zn-Ag$ deposits. Moreover, the strong correlation between Zn and MnO contents observed in Fig. 10a and b suggests that the presence of Zn-rich rhodonite in skarns could be used as a useful indicator for Zn mineralization when combined with other geological, geophysical and geochemical observations.

Conclusions

Based on the findings and interpretations discussed above, the following conclusions can be drawn:

1. The new $Sm-Nd$ isotopic data for the rhodonite−calcite pair yield an isochron age of 183 ± 2.3 Ma (MSWD = 0.72), showing that the Luziyuan deposit formed in the Early Jurassic. It is suggested that the Luziyuan $Pb-Zn$ mineralization could be related to eastward subduction of the Shan Boundary Ocean beneath the Baoshan block.
2. Zn enrichment in rhodonite could be controlled by Mn enrichment in the magmatic hydrothermal fluid, and skarn-hosted Zn-rich rhodonite is a potential indicator mineral for the exploration of base metal sulfide skarn deposits.

Author contribution Lin Ye and Yulong Yang conceived, designed and carried out the research. Yulong Yang drafted the manuscript. All authors contributed to data interpretation, discussion, and revision of the manuscript.

Availability of data and materials All data presented in the text of the article are fully available without restriction from authors upon request. Code availability is not applicable.

Declarations

References

Abrecht J (1985) Manganiferous pyroxenes and pyroxenoids from three $Pb-Zn-Cu$ skarn deposits. Contrib Mineral Petrol 89:379–393

Abrecht J, Peters T (1980) The miscibility gap between rhodonite and bustamite along the join $MnSiO_3$-$Ca_{0.60}$ $Mn_{0.40}SiO_3$. Contrib Mineral Petrol 74:261–269

Anders M, Grevesse N (1989) Abundances of the elements: meteoritic and solar. Geoch Cosmoch Act 53:197–214

Bau M (1996) Controls on the fractionation of isovalent trace elements in magmatic and aqueous systems: evidence from Y/Ho, Zr/Hf, and lanthanide tetrad effect. Contrib Mineral Petrol 123:323–333

Bradley DC, Leach DL, Symons D, Emsbo P, Premo W, Breit G, Sangster DF (2004) Reply to Discussion on ''Tectonic controls of Mississippi Valley-type lead–zinc mineralization in orogenic forelands'' by Kesler SE, Christensen JT, Hagni RD, Heijlen W, Kyle JR, Misra KC, Muchez P and van der Voo R. Min Dep 39(4):515–519

Burt DM (1977) Mineralogy and geochemistry of skarn deposits. Rendiconti Di Societá Italiana Di Mineralogia e Petrologia 33(2):859–873

Chen FC, Deng J, Shu QH, Li GJ, Cui XL, Zhao F, Wang QF (2017) Geology, fluid inclusion and stable isotopes (O, S) of the Hetaoping distal skarn $Zn-Pb$ deposit, northern Baoshan block, SW China. Ore Geol Rev 90:913–927

Chesley JT, Halliday AN, Kyser TK, Spry PG (1994) Direct Dating of Mississippi Valley-Type Mineralization: Use of Sm–Nd in Fluorite. Econ Geol 89(5):1192–1199

Christensen JN, Halliday AN, Leigh KE, Randell RN, Kesler SE (1995) Direct dating of sulfides by Rb–Sr: A critical test using the Polaris Mississippi Valley-type Zn–Pb deposit. Geoch Cosmoch Act 59(24):5191–5197

Deng J, Wang Q, Li G, Li C, Wang C (2014) Tethys tectonic evolution and its bearing on the distribution of important mineral deposits in the Sanjiang region, SW China. Gondwana Res 26:419–437

Deng MG, Li WC, Wen HJ, Cang FB, Wang P, Lü L, Xu R, Zeng L, Liu XL, Liu W, Yin GH (2013) The finding and prospecting significance of rhodonite in the Luziyuan lead–zinc polymetallic ore deposit in Zhenkang. Western Yunnan Geol Bull China 32(11):1867–1869 (in Chinese with English abstract)

Deng MG, Xu R, Wang P, Sun BD, Zeng L, Yu HJ, Wang T, Sha JZ (2016) Geochemistry of the rhodonite in the Luziyuan Pb–Zn–Fe polymetallic deposit in West Yunnan and their genesis significance. Act Petrol Sin 32(8):2248–2264 (in Chinese with English abstract)

Dong ML, Dong GC, Mo XX, Zhu DC, Nie F, Xie XF, Wang X, Hu ZC (2012) Geochronology and geochemistry of the Early Palaeozoic granitoids in Baoshan block, western Yunnan and their implications. Act Petrol Sin 28(5):1453–1464 (in Chinese with English abstract)

Dong WW, Chen SL (2007) The characteristics and genesis of Luziyuan Pb–Zn deposit, Zhenkang. Yunnan Geol 26:404–410 (in Chinese with English abstract)

Gaspar M, Knaack C, Meinert LD, Moretti R (2008) REE in skarn systems: a LA-ICP-MS study of garnets from the Crown Jewel gold deposit. Geoch Cosmoch Act 72:185–205

Halliday AN, Ohr M, Mezger K, Chesley JT, Nakai S, DeWolf CP (1991) Recent developments in dating ancient crustal fluid flow. Rev Geophys 29:577–584

Huang H, Zhang CQ, Zhou YM, Xie HF, Liu B, Xie YF, Dong YT, Yang CH, Dong WW (2014) Rb–Sr isochron age of Jinchanghe Fe–Cu–Pb–Zn polymetallic deposit in Yunnan Province and its geological significance. Mineral Depos 33(1):123–136 (in Chinese with English abstract)

Kempe U, Belyatsky B, Krymsky R, Kremenetsky A, Ivanov P (2001) Sm–Nd and Sr isotope systematics of scheelite from the giant Au(–W) deposit Muruntau (Uzbekistan): implications for the age and sources of Au mineralization. Mineral Depos 36(5):379–392

Li WC, Mo XX (2001) The Cenozoic tectonics and metallogenesis in the 'three-river' area of southwest China. Yunnan Geol 20:333–346 (in Chinese with English abstract)

Liu YS, Hu ZC, Gao S, Günther D, Xu J, Gao CG, Chen HH (2008) In situ analysis of major and trace elements of anhydrous minerals by LA-ICP-MS without applying an internal standard. Chem Geol 257:34–43

Ludwig KR (2003) ISOPLOT 3.00: A Geochronological Toolkit for Microsoft Excel. Berkeley Geochronology Center, California, Berkeley. 1–39

Lü CL, Deng MG, Hu W (2013) Study on metallogenic conditions and occurrence regularity of Luziyuan Pb–Zn deposit, Zhenkang Town, Yunnan Province. Contrib Geol Mineral Resour Res 28:529–534 (in Chinese with English abstract)

McCulloch MT, Compston W (1981) Sm–Nd age of Kambalda and Kanowna greenstones and heterogeneity in the Archean mantle. Nature 294:322–327

Meinert LD (1987) Skarn zonation and fluid evolution in the Groundhog Mine, Central mining district, New Mexico. Econ Geol 82:523–545

Meinert LD, Dipple GM, Nicolescu AS (2005) World skarn deposits. Econ Geol 100:299–336

Meinert LD, Hedenquist JW, Satoh H, Matsuhisa Y (2003) Formation of anhydrous and hydrous skarn in Cu–Au ore deposits by magmatic fluids. Econ Geol 98:147–156

Metcalfe I (2011) Tectonic framework and Phanerozoic evolution of Sundaland. Gondwana Res 19:3–21

Metcalfe I (2013) Gondwana dispersion and Asian accretion: tectonic and palaeogeographic evolution of eastern Tethys. J Asian Earth Sci 66:1–33

Morgan JW, Wandless GA (1980) Rare earth element distribution in some hydrothermal minerals: Evidence for crystallographic control. Geoch Cosmoch Act 44:973–980

Nakano T, Yoshino T, Shimazaki H, Shimizu M (1994) Pyroxene composition as an indicator in the classification of skarn deposits. Econ Geol 89(7):1567–1580

Nelson WR, Griffen DT (2005) Crystal chemistry of Zn-rich rhodonite ("fowlerite"). Am Mineral 90:969–983

Pan YM, Fleet ME (1996) Intrinsic and external controls on the incorporation of rare-earth elements in calc-silicate minerals. Can Mineral 34:147–159

Rudnick RL, Gao S (2003) Composition of the continental crust. Treatise Geochem 4:1–64

Shannon RD (1976) Revised effective ionic radii and systematic studies of interatomic distances in halides and calcogenides. Act Cryst A32:751–767

Su WC, Hu RZ, Xia B, Xia Y, Liu YP (2009) Calcite Sm–Nd isochron age of the Shuiyindong Carlin-type gold deposit, Guizhou, China. Chem Geol 258:269–274

Tao Y, Hu RZ, Zhu FL, Ma YS, Ye L, Cheng ZT (2010) Ore-forming age and the geodynamic background of the Hetaoping lead–zinc deposit in Baoshan, Yunnan. Act Petrol Sin 26:1760–1772 (in Chinese with English abstract)

Usuki T, Lan CY, Wang KL, Chiu HY (2012) Linking the Indochina craton and Gondwana during the Early Paleozoic: evidence from U-Pb ages and Hf isotopes of detrital zircons. Tectonophys 586:145–159

Wang CM, Deng J, John E, Carranza EJ, Santosh M (2014) Tin metallogenesis associated with granitoids in the southwestern Sanjiang Tethyan Domain: Nature, deposit types, and tectonic setting. Gondwana Res 26(2):576–593

Wang P (2016) Origin of the rhodonite from Luziyuan Pb-Zn mineral deposit in west Yunnan and its geological significance. Kunming Univ Sci Technol 1–73 (in Chinese with English abstract)

Whitney DL, Evans BW (2010) Abbreviations for names of rock-forming minerals. Am Mineral 95:185–187

Xiong CL, Jia XC, Yang XJ, Luo G, Bai XZ, Huang BX (2012) LA-ICP-MS zircon U-Pb dating of Ordovician Mengmao monzogranite in Longling area of western Yunnan Province and its tectonic setting. Geol Bull China 31(2/3):277–286 ((in Chinese with English abstract))

Xu R (2016) Isotope geochemistry characteristics and discussion on genesis of Luziyuan lead-zinc-iron polymetallic mineral deposit, Zhenkang, West Yunnan, China. Kunming Univ Sci Technol 1–87 (in Chinese with English abstract)

Xu R, Deng MG, Li WC, Lai CK, Zaw K, Gao ZW, Chen YH, Niu CH, Liang G (2020) Origin of giant Luziyuan Zn-Pb-Fe(-Cu) distal skarn deposit, Baoshan block, SE Tibet: Constraints from Pb–Sr isotopes, calcite C-O isotopes, trace elements and Sm–Nd dating. J Asian Earth Sci 205:1–24

Yang YL, Ye L, Bao T, Gao W, Li ZL (2018) Mineralization of Luziyuan Pb–Zn skarn deposit, Baoshan, Yunnan Province, SW China: evidence from petrography, fluid inclusions and stable isotopes. Geol Mag 156(4):639–658

Ye L, Gao W, Cheng ZT, Yang YL, Tao Y (2010) LA-ICP-MS zircon U-Pb geochronology and petrology of the Muchang alkali granite, Zhenkang County, Western Yunnan Province, China. Act Geol Sin 84:1488–1499

Zhao YM (1997) Metasomatic zoning in some major Pb–Zn polymetallic skarn deposits of china. Mineral Depos 16:121–129 (in Chinese with English abstract)

Zhao YM, Dong YG, Li DX, Bi CS (2003) Geology, mineralogy, geochemistry, and zonation of the Bajiazi dolostone-hosted Zn–Pb–Ag skarn deposit, Liaoning Province, China. Ore Geol Rev 223:153–182

Zhao ZF, Lu YX, Xie YH (2002) An example study of remote sensing and Gis metallogenetic prognosis inLuziyuan area, Zhenkang. Yunnan Geol 21:300–307 (in Chinese with English abstract)

Zhu FL, Tao Y, Hu RZ, Liao MY, Wang YX, Li YB (2011) Formation age of the Luziyuan lead–zinc deposit in Zhenkang, Yunnan. Bull Mineral Petrol Geochem 30(1):73–79 (in Chinese with English abstract)